PHOTONICS Research

Broadband mid-infrared second harmonic generation using epitaxial polydomain barium titanate thin films

JUNCHAO ZHOU,[1,2,3] WENRUI ZHANG,[4] MINGZHAO LIU,[4] AND PAO TAI LIN[1,2,3,*]

[1]*Department of Electrical and Computer Engineering, Texas A&M University, College Station, Texas 77843, USA*
[2]*Department of Materials Science and Engineering, Texas A&M University, College Station, Texas 77843, USA*
[3]*Center for Remote Health Technologies and Systems, Texas A&M University, College Station, Texas 77843, USA*
[4]*The Center for Functional Nanomaterials, Brookhaven National Laboratory, Upton, New York 11973, USA*
Corresponding author: paolin@ece.tamu.edu

The mid-infrared (mid-IR) second-order optical nonlinearity of the barium titanate (BTO) thin films was characterized by second harmonic generation (SHG). The epitaxial BTO thin films were grown on strontium titanate substrates by pulsed-laser deposition. From the azimuthal-dependent polarized SHG measurements, the tensorial optical nonlinear coefficients, d_{ij}, and ferroelectric domain fraction ratio, $\delta A_Y / \delta A_z$, were resolved. Strong SHG signals were obtained at the pumping laser wavelength λ between 3.0 and 3.6 μm. The SHG intensity was linearly dependent upon the square of the pumping laser power. The broadband mid-IR optical nonlinearity enables BTO thin films for applications in chip-scale quantum optics and nonlinear integrated photonic circuits.   ©2019 Chinese Laser Press

https://doi.org/10.1364/PRJ.7.001193

1. INTRODUCTION

Perovskite oxides, such as $LiNbO_3$, $KNbO_3$, and $BaTiO_3$, are attractive materials because they exhibit excellent ferroelectric and nonlinear optical properties at room temperature. Their ferroelectric properties lead to a variety of applications including sensors [1], non-volatile memory devices [2], and optical communications [3,4]. Perovskite oxides have the chemical formula ABO_3, where their polar property determines the polarization, which is the net dipole moment in the unit volume. The nonlinear interactions between the electric dipole and light waves create nonlinear optical responses such as SHG, sum-frequency generation (SFG), difference-frequency generation (DFG), and optical parametric oscillation (OPO) [5]. One application for nonlinear optic technology is to provide light sources over ultraviolet, visible, infrared, and THz bands through nonlinear light conversion [6–8]. Another critical application for nonlinear optic technology includes quantum optics, where entangled photon pairs are efficiently created during the nonlinear optical processes [9–11].

Though bulk crystalline perovskite oxides have a strong optical nonlinearity, a thin film form is required to monolithically integrate these perovskites with photonic circuits. Perovskite oxide thin films can be grown by numerous epitaxy techniques such as metal oxide chemical vapor deposition (MOCVD), molecule-beam epitaxy (MBE), and pulsed-laser deposition (PLD) [12–14]. Among these perovskite oxide thin films, BTO has

attracted much attention and been utilized in various micro- and nano-photonic devices for the following reason [15–18]: BTO thin films have a broad transparent window in visible and IR range [19,20]. Through the Pockels effect, the refractive indexes of BTO thin films are tunable by applying external electric fields [21,22]. The second-order nonlinear susceptibilities of BTO can be further enhanced by inducing stress in the BTO thin film [23]. Moreover, BTO thin films can be epitaxially grown on the Si substrates with an intermediate buffer layer [24,25], thus providing additional functionality for present Si photonic devices.
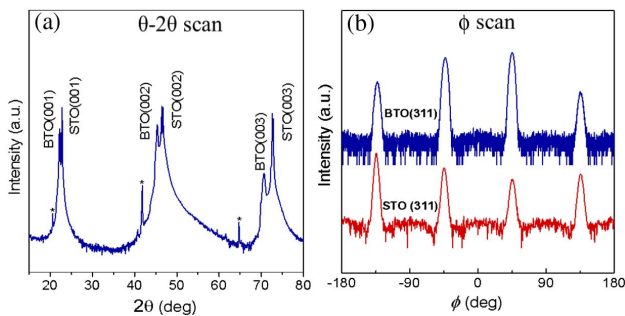
The optical nonlinearity of BTO thin films has been explored in the visible and near-IR regions [26–28], while not in the mid-IR region, which is an important spectrum for the development of optical networking [29], biomedical sensing [30], molecular spectroscopy [31], and thermal imaging [32]. For optical communication, a broader spectrum extending into the mid-IR region can accommodate additional channels for high-speed data transmission. Moreover, mid-IR sensing enables label-free and non-destructive molecule detection [33,34]. In this study, the epitaxial BTO thin films were deposited onto a strontium titanate (STO) substrate by PLD. Polarization-dependent mid-IR SHG was measured and analyzed to resolve the optical nonlinear coefficients and the ferroelectric a/c domain distribution. Our results illustrated that the epitaxial BTO thin film is an ideal platform for mid-IR nonlinear integrated photonics.

2. EPITAXIAL BTO THIN FILM GROWTH AND XRD CHARACTERIZATION

The BTO thin film was deposited onto a single-crystal STO (001) substrate by PLD at 600°C and 20 mTorr of O_2. The PLD used a KrF excimer laser ($\lambda = 248$ nm) with a fluence of 1.5 J/cm^2 and a repetition rate of 5 Hz. The BTO target was prepared by a conventional ceramic sintering method. The grown BTO film was 500-nm thick with a uniform surface. The crystalline structure of the BTO thin film was characterized by X-ray diffraction (XRD). From the θ-2θ scan in Fig. 1(a), only BTO (00l) was found, indicating that the BTO thin film is a single crystalline film and mainly grown along the (00l) direction. The φ scans of BTO (113) and STO (113) in Fig. 1(b) indicate that the BTO thin film exhibited cube-on-cube growth on the STO substrate without experiencing in-plane rotations.
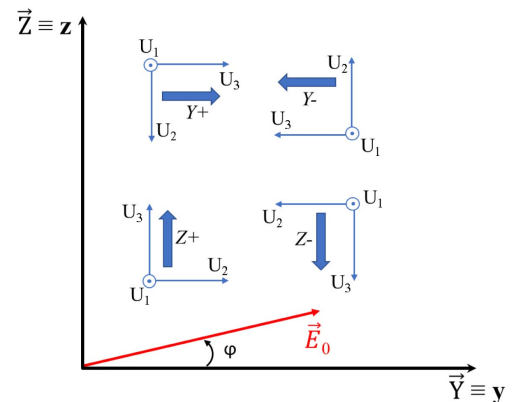
3. MODELING OF THE MID-IR SHG FROM BTO THIN FILMS

A BTO crystal possesses different crystal symmetries at different temperatures due to its phase transitions. Upon increasing the temperature, the phase of the BTO crystal changes sequentially from rhombohedral to orthorhombic, tetragonal (at 0–120°C), and paraelectric cubic phase. The space group of tetragonal BTO is $P4mm$ and its unit cell is slightly elongated along the c-direction, which is the fourfold axis as shown in Fig. 2(a).

The distance from the center Ti atom to the O atoms along the c-axis can be greater or smaller than to the other O atoms along the a-axis, leading to a spontaneous polarization P_s parallel to the c-axis [35]. For an epitaxial BTO thin film, the coordinate axes were defined by the crystal axes of the STO substrate. As shown in Fig. 2(b), the [001], [100], and [010] axes of the STO are defined as the $+\vec{X}$, $+\vec{Y}$, and $+\vec{Z}$ axes, respectively. A BTO thin film can have six different ferroelectric domain variants with their polarizations parallel to the $+\vec{X}$, $-\vec{X}$, $+\vec{Y}$, $-\vec{Y}$, $+\vec{Z}$, and $-\vec{Z}$ directions, which are labeled as the $X+$, $X-$, $Y+$, $Y-$, $Z+$, and $Z-$ domains, respectively. To study the polarimetric SHG, Fig. 3 illustrates that the x, y, and z axes of the lab coordination are initially aligned to the $+\vec{X}$, $+\vec{Y}$, and $+\vec{Z}$ axes defined by the crystal coordination of the STO substrate [36]. In other words, a light beam E^ω propagating along the x-axis is normally incident to the (001) surface of the STO substrate, and its polarization is in the y–z plane. At azimuth $\varphi = 0$, the polarization direction is coincident with the y-axis. To analyze the polarimetric SHG from a multi-domain BTO thin film, a polarizer was placed before the photodetector to differentiate the y and z polarized SHG signals, where the intensities are denoted as $I_y^{2\omega}$ and $I_z^{2\omega}$, respectively. For E^ω propagating in the x-direction,

Fig. 1. XRD results of the BTO thin film deposited on the (001) STO substrate by PLD. (a) A θ-2θ scan of the BTO thin film. The BTO was epitaxially grown along the (00l) direction. (b) A φ scan of the BTO thin film indicated a cube-on-cube growth on the STO substrate.

Fig. 3. Four possible domain variants in the y–z plane, $Y+$, $Y-$, $Z+$, and $Z-$, and the crystal axes (U_1, U_2, U_3) associated with each of the four domain variants. The incident light $\vec{E}_0$ is linearly polarized, and the azimuthal angle between the incident light and the y-axis is noted as φ.
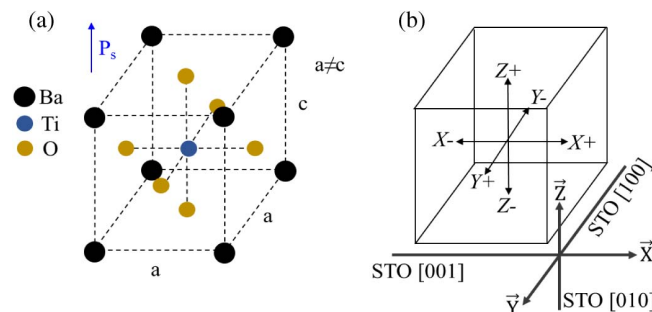
Fig. 2. (a) Structure of a tetragonal BTO unit cell with one Ti atom in the cell center, eight Ba atoms in the corners, and six O atoms in the center of the facets. (b) The six possible ferroelectric domain variants, $X+$, $X-$, $Y+$, $Y-$, $Z+$, and $Z-$, in the $+\vec{X}$, $+\vec{Y}$, and $+\vec{Z}$ lab-based coordinate system.

the $X+$ and $X-$ domain variants will not create an SHG polarization in the y–z plane.

The SHG collected from a multi-domain BTO thin film was considered as a combination of the SHG signals attributed by each domain variant. To use the nonlinear optical tensor matrix, the components of the incident electric field (E_x, E_y, E_z) were transformed and interpreted by the orthogonal crystal coordination (U_1, U_2, U_3) corresponding to each domain variant. Here, the optic axis of the crystal U_3 is parallel to the direction of P_s and equivalent to the c-axis indicated in Fig. 2(a).

Figure 3 displays the new coordinations (U_1, U_2, U_3) and the P_s direction associated with the $Y+$, $Y-$, $Z+$, and $Z-$ domain variants, separately. The second-order nonlinear polarization for the tetragonal BTO is then described as

$$P_s = \begin{pmatrix} P_1 \\ P_2 \\ P_3 \end{pmatrix} = \begin{pmatrix} 0 & 0 & 0 & 0 & d_{15} & 0 \\ 0 & 0 & 0 & d_{15} & 0 & 0 \\ d_{31} & d_{31} & d_{33} & 0 & 0 & 0 \end{pmatrix} \begin{pmatrix} E_1^2 \\ E_2^2 \\ E_3^2 \\ 2E_2E_3 \\ 2E_1E_3 \\ 2E_1E_2 \end{pmatrix}. \tag{1}$$

E_1, E_2, and E_3 are the components of the electrical fields along the U_1, U_2, and U_3 axes, and d_{ij} is the tensor element of the second-order optical nonlinear coefficients. The electric field of the light propagating along the x-direction has $E_x = 0$, $E_y = E_0 \cos\varphi$, and $E_z = E_0 \sin\varphi$. Considering the $Y+$ domain, the electric fields represented by the domain coordination became $E_1 = E_x = 0$, $E_2 = -E_z = -E_0 \sin\varphi$, and $E_3 = E_y = E_0 \cos\varphi$. Hence, by applying this to Eq. (1), the nonlinear polarizations from the $Y+$ domain are expressed as

$$P_1^{Y+} = 2d_{15}E_1E_3 = 0, \tag{2}$$

$$P_2^{Y+} = 2d_{15}E_2E_3 = -E_0^2 d_{15} \sin 2\varphi, \tag{3}$$

$$\begin{aligned} P_3^{Y+} &= d_{31}E_1^2 + d_{31}E_2^2 + d_{33}E_3^2 \\ &= E_0^2 d_{31} \sin^2\varphi + E_0^2 d_{33} \cos^2\varphi. \end{aligned} \tag{4}$$

In addition, the SHG intensity, I, is proportional to $P \times P^*$, and for the $Y+$ domain, y and z are parallel to U_3 and U_2, respectively. Therefore, it follows that

$$I_y^{2\omega} \propto P_3^2 = (E_0^2 d_{31} \sin^2\varphi + E_0^2 d_{33} \cos^2\varphi)^2, \tag{5}$$

$$I_z^{2\omega} \propto P_2^2 = (E_0^2 d_{15} \sin 2\varphi)^2. \tag{6}$$

The reported SHG coefficients of bulk BTO crystal at $\lambda = 1060$ nm are $d_{15} = 17$ pm/V, $d_{31} = 15.7$ pm/V, and $d_{33} = 6.8$ pm/V [23]. Figure 4 plots the y and z polarized SHG signals created from the $Y+$ domain when the incident light polarization was rotated along φ on the y–z plane. $I_y^{2\omega}$ exhibited a two-lobed intensity profile, while $I_z^{2\omega}$ had a distinguishable four-lobed profile. Similarly, the nonlinear polarizations contributed by the $Y+$, $Y-$, $Z+$, and $Z-$ domains were calculated and represented by the domain coordinates, which are summarized as
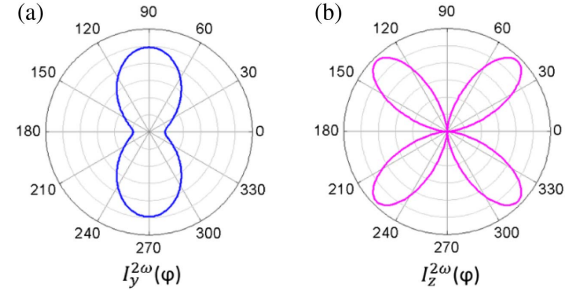
Fig. 4. Calculated azimuthal-dependent polarized SHG, $I_y^{2\omega}(\varphi)$ and $I_z^{2\omega}(\varphi)$, of a single $Y+$ domain BTO thin film. The tensors d_{ij} from a bulk BTO crystal were used: $d_{15} = 17$ pm/V, $d_{31} = 15.7$ pm/V, and $d_{33} = 6.8$ pm/V. The thickness of the BTO crystal was 500 nm. $I_y^{2\omega}(\varphi)$ and $I_z^{2\omega}(\varphi)$ showed distinct two-lobed and four-lobed SHG patterns, respectively.

$$P_1^{Y+} = P_1^{Y-} = P_1^{Z+} = P_1^{Z-} = 0, \tag{7}$$

$$P_2^{Y+} = P_2^{Y-} = -P_2^{Z+} = -P_2^{Z-} = -E_0^2 d_{15} \sin 2\varphi, \tag{8}$$

$$P_3^{Y+} = P_3^{Y-} = E_0^2 d_{31} \sin^2\varphi + E_0^2 d_{33} \cos^2\varphi, \tag{9}$$

$$P_3^{Z+} = P_3^{Z-} = E_0^2 d_{31} \cos^2\varphi + E_0^2 d_{33} \sin^2\varphi. \tag{10}$$

When the pump light passed through a BTO thin film containing different ferroelectric domains, the SHG contributed by each of these domains needs to be considered. The area fractions of each domain are defined as A^{Y+}, A^{Y-}, A^{Z+}, and A^{Z-}, where the sum of all the area fractions is 1. From the transformation between the domain variants and the lab coordinates shown in Fig. 2, it was concluded that $P_y^{Y+} = P_3^{Y+}$, $P_y^{Y-} = -P_3^{Y-}$, $P_y^{Z+} = P_2^{Z+}$, and $P_y^{Z-} = -P_2^{Z-}$. Using Eqs. (7)–(10), the total nonlinear polarization $P_y^{2\omega}$ created by the four domains, $Y+$, $Y-$, $Z+$, and $Z-$, is

$$\begin{aligned} P_y^{2\omega} &= A^{Y+}P_y^{Y+} + A^{Y-}P_y^{Y-} + (A^{Z+}P_y^{Z+} + A^{Z-}P_y^{Z-})e^{i\Gamma} \\ &= A^{Y+}P_3^{Y+} - A^{Y-}P_3^{Y-} + (A^{Z+}P_2^{Z+} - A^{Z-}P_2^{Z-})e^{i\Gamma} \\ &= \delta A_Y P_3^{Y+} + \delta A_Z P_2^{Z+} e^{i\Gamma}. \end{aligned} \tag{11}$$

δA_Y and δA_Z are defined as $\delta A_Y = A^{Y+} - A^{Y-}$ and $\delta A_Z = A^{Z+} - A^{Z-}$, which present the difference in the area fractions between the domain pairs, such as ($Y+$, $Y-$) and ($Z+$, $Z-$), oriented along the opposite directions. From Eq. (11), $P_y^{2\omega}$ is strongly correlated with the domain orientation and the domain fraction of the opposite polarization. Due to the difference of the refractive indexes along the c- and a-axes of the BTO, a phase term $\Gamma = (2\pi l/\lambda)(n_c^{2\omega} - n_a^{2\omega})$ was added to Eq. (11) to account for the birefringence between the c- and a-axes. Here, l is the thickness of the thin film sample, and $n_c^{2\omega}$ and $n_a^{2\omega}$ are the refractive indexes at the second harmonic frequency 2ω along the c- and a-axes of BTO, respectively. If these four domains have equal areas, no SHG signal will be observed because δA_Y and δA_Z become zero in Eq. (11). Since $I_y^{2\omega} \propto P_y^{2\omega}(P_y^{2\omega})^*$, the SHG intensity of the y-polarization is

$$I_y^{2\omega} \propto \delta A_Y^2 (P_3^{Y+})^2 + \delta A_Z^2 (P_2^{Z+})^2 \pm 2\delta A_Y \delta A_Z P_3^{Y+} P_2^{Z+} \cos\Gamma$$

$$= \delta A_Y^2 (d_{31} \sin^2\varphi + d_{33} \cos^2\varphi)^2 + \delta A_z^2 (d_{15} \sin 2\varphi)^2$$

$$+ 2\delta A_Y \delta A_Z (d_{31} \sin^2\varphi + d_{33} \cos^2\varphi) d_{15} \sin 2\varphi \cos\Gamma.$$

$$(12)$$

For convenience, the value of E_0 was set to 1. The expression of y-polarized SHG is then rewritten as

$$I_y^{2\omega} = K_{1,y}(\cos^2\varphi + K_{2,y} \sin^2\varphi)^2 + K_{3,y} \sin^2 2\varphi$$

$$+ K_{4,y}(\cos^2\varphi + K_{2,y} \sin^2\varphi) \sin 2\varphi, \qquad (13)$$

where $K_{1,y} = \delta A_Y^2 d_{33}^2$, $K_{2,y} = d_{31}/d_{33}$, $K_{3,y} = \delta A_Z^2 d_{15}^2$, and $K_{4,y} = 2\delta A_Y \delta A_Z d_{15} d_{33} \cos\Gamma$.

Using the same approach, the intensity of the z-polarized SHG $I_z^{2\omega}$ is

$$I_z^{2\omega} = K_{1,z}(\cos^2\varphi + K_{2,z} \sin^2\varphi)^2 + K_{3,z} \sin^2 2\varphi$$

$$+ K_{4,z}(\cos^2\varphi + K_{2,z} \sin^2\varphi) \sin 2\varphi, \qquad (14)$$

where $K_{1,z} = \delta A_Z^2 d_{31}^2$, $K_{2,z} = d_{33}/d_{31}$, $K_{3,z} = \delta A_Y^2 d_{15}^2$, and $K_{4,z} = 2\delta A_Y \delta A_Z d_{15} d_{31} \cos\Gamma$. The parameters $K_{i,j}$ derived from the x and y polarizations have the following relations:

$$\cos^2\Gamma = \frac{K_{4,y}^2}{4K_{1,y}K_{3,y}} = \frac{K_{4,z}^2}{4K_{1,z}K_{3,z}} \qquad (15)$$

and

$$\frac{d_{33}}{d_{31}} = K_{2,z} = \frac{1}{K_{2,y}}. \qquad (16)$$

The SHG intensity can be calculated by Eqs. (13) and (14) when all the $K_{i,j}$ are known. On the other hand, $K_{i,j}$ and the associated material parameters, including the domain fraction difference δA and nonlinear coefficient d_{ij}, can be extrapolated by fitting the experimentally obtained SHG. In parallel, Eqs. (15) and (16) establish the relationship between the eight $K_{i,j}$ identities and validate the model used to interpret the domain orientation and the optical nonlinearity.

Hence, the polarimetric response of the SHG is determined by the domain fraction ratio $\delta A_Y/\delta A_Z$ and the optical nonlinearity d_{ij}. To examine the effect of $\delta A_Y/\delta A_Z$, Figs. 5(a)–5(c) show the calculated angular-dependent $I_y^{2\omega}(\varphi)$ and $I_z^{2\omega}(\varphi)$ by applying Eqs. (13) and (14) at $\delta A_Y/\delta A_Z = 10$, 1, and 0.1, respectively. The values of the optical nonlinear coefficients, $d_{15} = 17$ pm/V, $d_{31} = 15.7$ pm/V, and $d_{33} = 6.8$ pm/V, were obtained from a bulk BTO crystal. As shown in Fig. 5(a), at $\delta A_Y/\delta A_Z = 10$, the Y domains were the dominant factor for the polarimetric SHG pattern, resulting in a two-lobed $I_y^{2\omega}$ profile and a four-lobed $I_z^{2\omega}$ profile. The two-lobed $I_y^{2\omega}$ had its maximum SHG intensity at $\varphi = 80°$ and $260°$. On the other hand, the four-lobed $I_z^{2\omega}$ had its maximum SHG intensity at $\varphi = 45°$ and $235°$, and its other two peaks had maximum SHG intensities at $\varphi = 135°$ and $315°$. The SHG patterns at $\delta A_Y/\delta A_Z = 10$ were similar to the SHG patterns in Fig. 4, which were created from a single $Y+$ domain BTO, except that the two lobes of the $I_y^{2\omega}(\varphi)$ were slightly tilted away from the vertical axis, and the maximum SHG intensities from those four lobes in $I_y^{2\omega}(\varphi)$ were different. When $\delta A_Y/\delta A_Z$ was decreased to 1, the Y and Z domains had comparable contributions to the SHG, thus creating $I_y^{2\omega}$ and
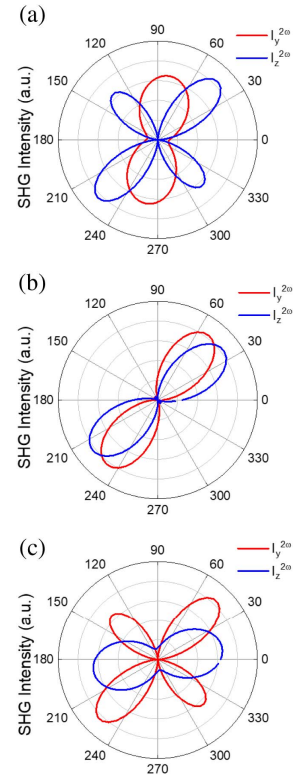

Fig. 5. $I_y^{2\omega}(\varphi)$ and $I_z^{2\omega}(\varphi)$ were calculated when the ferroelectric domain fraction ratio, $\delta A_Y/\delta A_Z$, was set to (a) 10, (b) 1, and (c) 0.1. The d_{ij} values were from a bulk BTO crystal. At $\delta A_Y/\delta A_Z = 10$, $I_y^{2\omega}(\varphi)$ had a two-lobed profile, and $I_z^{2\omega}(\varphi)$ had a four-lobed profile. As $\delta A_Y/\delta A_Z$ decreased to 0.1, $I_y^{2\omega}(\varphi)$ became four-lobed and $I_z^{2\omega}(\varphi)$ became two-lobed. In addition, the axis of the two-lobes rotated as $\delta A_Y/\delta A_Z$ changed.

$I_z^{2\omega}$ patterns with similar profiles as shown in Fig. 5(b). Both $I_y^{2\omega}(\varphi)$ and $I_z^{2\omega}(\varphi)$ have two lobes, and these lobes are approximately 45° away from the horizontal axis. Once $\delta A_Y/\delta A_Z$ was further decreased to 0.1, the Z domains became the dominant factor for the polarimetric SHG pattern. As a result, a four-lobed $I_y^{2\omega}$ profile and a two-lobed $I_z^{2\omega}$ profile were found and are illustrated in Fig. 5(c). Unlike Fig. 5(a) where the two lobes from $I_y^{2\omega}(\varphi)$ were closely aligned to the vertical axis, the other two lobes from $I_z^{2\omega}(\varphi)$ in Fig. 5(c) were almost aligned with the horizontal axis. Therefore, the symmetry and the angular dependence of the polarimetric SHG patterns are highly dependent on the domain fraction ratio. In other words, $\delta A_Y/\delta A_Z$ can be resolved by examining the variation of the $I_{y,z}^{2\omega}(\varphi)$ profiles.

4. POLARIMETRIC MID-IR SHG MEASUREMENTS

A. Experimental Setup

Figure 6 shows the schematic of the experimental setup for measuring the polarimetric SHG from a BTO thin film. A wavelength-tunable OPO pulsed laser was used as the mid-IR light source. The pulse repetition rate was 1 kHz, and the linewidth was smaller than 10 cm^{-1}. A bandpass filter with a transmission window from $\lambda = 3.25$ to 3.75 μm was placed after the laser. The maximum transmission was 80%
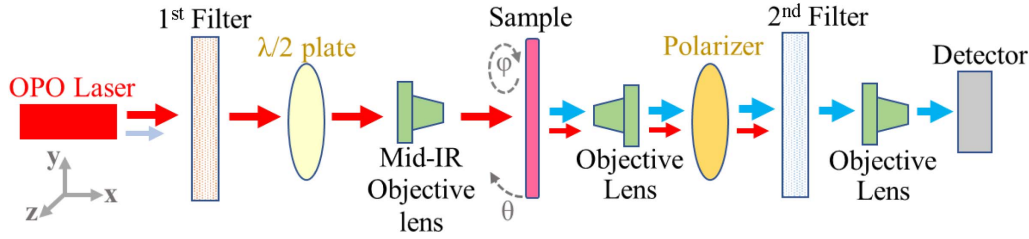
Fig. 6. Schematic of the experimental setup for measuring the azimuthal-dependent polarized SHG from a BTO thin film. The pumping laser was a tunable ns pulsed laser and the first filter removed the light that was not at the pumping wavelength λ. The polarization of the light was rotated by the $\lambda/2$ phase plate. The mid-IR light was focused on the BTO thin film using the front objective lens, and the SHG was collected by another objective lens in the back. The polarizer selected the polarization of the SHG signals, and the second filter removed the residual mid-IR pumping light. The SHG in the NIR region was measured by a photodetector or a spectrometer.

at $\lambda = 3.50$ μm. This filter was used to block the light frequencies other than the laser beam that had a pumping frequency of ω. After the first bandpass filter, the laser beam was focused onto the sample surface through a mid-IR objective lens to maximize the incident light intensity. The focusing length and the numerical aperture of the mid-IR objective lens were 6 mm and 0.25, respectively. The incident laser beam was projected along the x-direction. By rotating the half-wave plate, the polarization of the laser beam was also rotated by an azimuth angle φ along the x-axis. The half-wave plate had a 100% transmission and 1.5 wave retardance at $\lambda = 3.5$ μm. The BTO thin film sample was initially placed on a rotating stage to align the sample axes with the lab axes, so that $x/\!/[001]_{STO}$, $y/\!/[100]_{STO}$, and $z/\!/[010]_{STO}$. Otherwise, there will be an angle α between the principle c-axis of the BaTiO$_3$ sample and the lab coordinate y-axis. The angle between the lab coordinate y-axis and the direction normal to the BTO thin film surface is $\theta = 90°$ so that the input light was normally incident to the sample. To effectively collect all of the SHG signal, the light emitted from the BTO sample was collected and then refocused into a detector by two separate objective lenses. An ultra-broadband wire-grid polarizer operational at $\lambda = 0.25$–4 μm was placed after the objective lens as an analyzer to differentiate the polarized SHG, $I_y^{2\omega}$ or $I_z^{2\omega}$. The extinction ratio of the wire-grid polarizer was 10:1. A second bandpass filter with a transmission window from $\lambda = 1.5$ to 2.0 μm was placed in front of the detector to remove the remaining incident laser beam at frequency ω. Thus, only the generated SHG signal at 2ω was collected. The detector was a PbSe fixed gain photodetector sensitive from $\lambda = 1.5$ to 4.8 μm with a bandwidth range from 0.2 Hz to 10 kHz. The detector was connected to an oscilloscope, and the SHG signal at various φ was recorded from the amplitude of the pulse displayed on the oscilloscope.

B. Mid-IR Second-Order Optical Nonlinearity and Ferroelectric Domain Fractions

To investigate the optical nonlinearity and the ferroelectric domains of the BTO thin film, the azimuthal-dependent SHG signals along the y and z polarizations, $I_y^{2\omega}(\varphi)$ and $I_z^{2\omega}(\varphi)$, were measured and displayed in Figs. 7(a) and 7(b), respectively. The substrate STO had no second-order nonlinearity due to its crystal symmetry. Both y and z polarized SHG patterns show a dominant two-lobed profile with a pair of smaller lobes. For $I_y^{2\omega}(\varphi)$, the maximum SHG signal was found at a relative
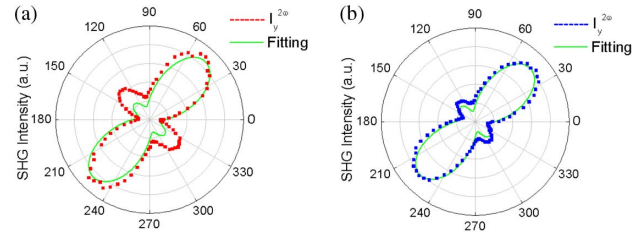

Fig. 7. (a) $I_y^{2\omega}(\varphi)$ and (b) $I_z^{2\omega}(\varphi)$ obtained from the BTO thin film deposited by PLD. The dashed lines represent the measured data and the solid green lines represent the modeling results. From the fitting, the values $d_{15} = 12.5$ pm/V, $d_{31} = 9.0$ pm/V, $d_{33} = 10.0$ pm/V, and $\delta A_Y/\delta A_Z = 1$ were resolved.

$\varphi = 45°$ and $135°$. The smaller lobes were found to be normal to the larger lobes. Similar profiles were observed for $I_z^{2\omega}(\varphi)$, where a pair of larger lobes and another pair of secondary lobes were found. A minor difference between the $I_y^{2\omega}(\varphi)$ and $I_z^{2\omega}(\varphi)$ is that the intensities of the secondary lobes were comparatively weaker in $I_z^{2\omega}(\varphi)$ than in $I_y^{2\omega}(\varphi)$. The SHG profiles shown in Fig. 7 were fitted by Eqs. (13) and (14). Accordingly, $d_{15} = 12.5$ pm/V, $d_{31} = 9.0$ pm/V, $d_{33} = 10.0$ pm/V, and $\delta A_Y/\delta A_Z = 1$ were obtained. The fitting results were consistent with the observation shown in Fig. 4, where $I_z^{2\omega}(\varphi)$ and $I_y^{2\omega}(\varphi)$ revealed a two-lobed dominant pattern when $\delta A_Y/\delta A_Z$ approached 1. In addition, the difference in d_{ij} between a bulk BTO crystal and the BTO thin film is due to the film strain introduced during PLD growth. A similar effect has been observed in studies using other perovskite oxides including SrTiO$_3$ and BaZrO$_3$ [37].

C. Mid-IR SHG Dependence on the Pumping Light Intensity

The variation of the SHG at different pumping light intensities was investigated. During the measurement, the laser power I_{laser} was gradually increased from 16 to 92 mW. The laser wavelength was $\lambda = 3.5$ μm and the azimuth angle φ was fixed at 45° because $I_y^{2\omega}(\varphi)$ reached its maximum at 45° according to Fig. 7(a). Figure 8 displays the SHG intensity versus the square of the pumping light intensity, $(I_{laser})^2$, where I_{laser} was measured by a digital optical power meter (Thorlabs PM100D). The SHG intensity increased proportionally to $(I_{laser})^2$ when I_{laser} gradually increased from 16 to 92 mW.
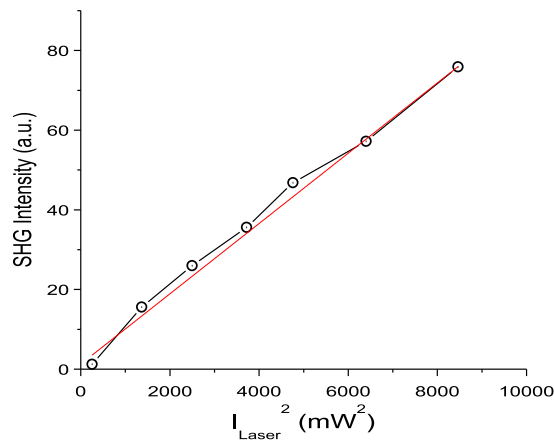
Fig. 8. SHG intensity, $I_y^{2\omega}$, versus the square of the input mid-IR laser power, I_{laser}, measured at $\lambda = 3.5$ μm. The black circles indicate the measured data, and the red line represents the fitted curve. A linear relationship between $I_y^{2\omega}$ and $(I_{laser})^2$ was found.

The mid-IR SHG pump threshold was 7 mW. The linear dependence obtained between $I_y^{2\omega}$ and $(I_{laser})^2$ agrees with the derivation illustrated in Eqs. (5) and (6).

D. Mid-IR SHG Spectral Characterization

The SHG spectrum from the BTO thin film was measured when the wavelength of the pumping laser was tuned over a range between $\lambda^\omega = 3.0$ and 3.6 μm. The SHG signal was collected by a 400 μm core diameter fiber and analyzed by a spectrometer that had a thermoelectric cooling InGaAs linear array. The azimuthal angle φ and the position of the BTO sample were fixed when the input wavelength was tuned. As drawn in Fig. 9, the center wavelength of the SHG spectrum increased from $\lambda^{2\omega} = 1.5$ to 1.8 μm when the laser pumping wavelength increased from $\lambda^\omega = 3.0$ to 3.6 μm. The slight broadening of
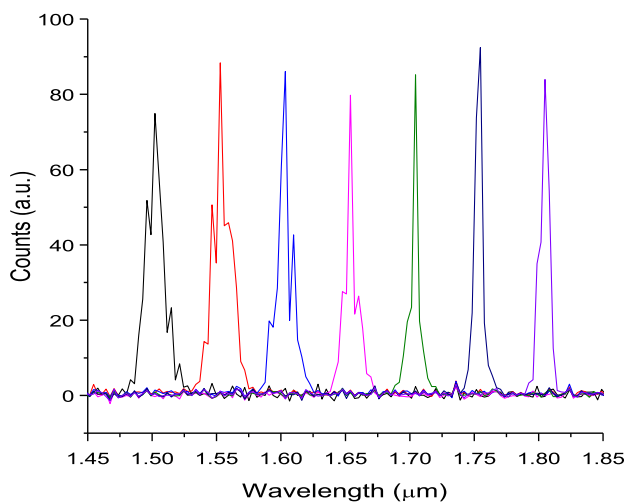
Fig. 9. SHG spectrum of the BTO thin film when the mid-IR pumping wavelength was tuned from $\lambda^\omega = 3.0$ to 3.6 μm. Strong SHG signals between $\lambda^{2\omega} = 1.5$ and 1.8 μm were found, indicating that BTO has a broadband second-order optical nonlinearity.

the SHG spectrum at $\lambda^{2\omega} < 1.65$ μm was due to variation in the pumping laser linewidth. The spectral scanning of the SHG signals demonstrates that the deposited BTO thin film can convert mid-IR signals over a wide spectrum efficiently into the NIR region, thus enabling on-chip and broadband nonlinear frequency conversion.

5. CONCLUSIONS

Broadband mid-IR SHG was demonstrated by an epitaxial BTO thin film on a (001) STO substrate using PLD. From XRD characterization, the BTO film had cube-on-cube growth mainly along the (00l) direction. The mid-IR optical nonlinearity and the ferroelectric domain property were characterized by azimuthal-dependent polarized SHG measurements. Two-lobed dominant $I_{x,y}^{2\omega}(\varphi)$ patterns were found in both polarizations. High nonlinear coefficients of $d_{15} = 12.5$ pm/V, $d_{31} = 9.0$ pm/V, and $d_{33} = 10.0$ pm/V, and a uniform domain fraction ratio of $\delta A_Y / \delta A_Z = 1$ were resolved. In addition, the characteristic SHG response, $I^{2\omega} \propto (I^\omega)^2$, and broadband SHG signals were observed at pumping wavelengths $\lambda^\omega = 3.0$–3.6 μm. The efficient nonlinear thin film paves the way for developing efficient on-chip light sources and integrated quantum photonics.

REFERENCES

1. D. Damjanovic, P. Muralt, and N. Setter, "Ferroelectric sensors," IEEE Sens. J. **1**, 191–206 (2001).
2. A. Chanthbouala, A. Crassous, V. Garcia, K. Bouzehouane, S. Fusil, X. Moya, J. Allibe, B. Dlubak, J. Grollier, S. Xavier, C. Deranlot, A. Moshar, R. Proksch, N. D. Mathur, M. Bibes, and A. Barthelemy, "Solid-state memories based on ferroelectric tunnel junctions," Nat. Nanotechnol. **7**, 101–104 (2012).
3. D. Sando, Y. Yang, C. Paillard, B. Dkhil, L. Bellaiche, and V. Nagarajan, "Epitaxial ferroelectric oxide thin films for optical applications," Appl. Phys. Rev. **5**, 041108 (2018).
4. C. Xiong, W. H. P. Pernice, J. H. Ngai, J. W. Reiner, D. Kumah, F. J. Walker, C. H. Ahn, and H. X. Tang, "Active silicon integrated nanophotonics: ferroelectric BaTiO₃ devices," Nano Lett. **14**, 1419–1425 (2014).
5. N. Bloembergen, Nonlinear Optics, 4th ed. (World Scientific, 1996).
6. A. Hermans, C. Kieninger, K. Koskinen, A. Wickberg, E. Solano, J. Dendooven, M. Kauranen, S. Clemmen, M. Wegener, C. Koos, and R. Baets, "On the determination of χ⁽²⁾ in thin films: a comparison of one-beam second-harmonic generation measurement methodologies," Sci. Rep. **7**, 44581 (2017).
7. L. E. Myers, R. C. Eckardt, M. M. Fejer, R. L. Byer, W. R. Bosenberg, and J. W. Pierce, "Quasi-phase-matched optical parametric oscillators in bulk periodically poled LiNbO₃," J. Opt. Soc. Am. B **12**, 2102–2116 (1995).

8. M. A. Belkin, F. Capasso, A. Belyanin, D. L. Sivco, A. Y. Cho, D. C. Oakley, C. J. Vineis, and G. W. Turner, "Terahertz quantum-cascade-laser source based on intracavity difference-frequency generation," Nat. Photonics **1**, 288–292 (2007).

9. H. Jin, F. M. Liu, P. Xu, J. L. Xia, M. L. Zhong, Y. Yuan, J. W. Zhou, Y. X. Gong, W. Wang, and S. N. Zhu, "On-chip generation and manipulation of entangled photons based on reconfigurable lithium-niobate waveguide circuits," Phys. Rev. Lett. **113**, 103601 (2014).

10. S. Arahira, N. Namekata, T. Kishimoto, H. Yaegashi, and S. Inoue, "Generation of polarization entangled photon pairs at telecommunication wavelength using cascaded $\chi^{(2)}$ processes in a periodically poled LiNbO$_3$ ridge waveguide," Opt. Express **19**, 16032–16043 (2011).

11. O. Alibart, V. D'Auria, M. De Micheli, F. Doutre, F. Kaiser, L. Labonté, T. Lunghi, É. Picholle, and S. Tanzilli, "Quantum photonics at telecom wavelengths based on lithium niobate waveguides," J. Opt. **18**, 104001 (2016).

12. J. Wang, J. B. Neaton, H. Zheng, V. Nagarajan, S. B. Ogale, B. Liu, D. Viehland, V. Vaithyanathan, D. G. Schlom, U. V. Waghmare, N. A. Spaldin, K. M. Rabe, M. Wuttig, and R. Ramesh, "Epitaxial BiFeO$_3$ multiferroic thin film heterostructures," Science **299**, 1719–1722 (2003).

13. K. Suzuki, D. Fu, K. Nishizawa, T. Miki, and K. Kato, "Ferroelectric property of alkoxy-derived YMnO$_3$ films crystallized in argon," Jpn. J. Appl. Phys. **42**, 5692–5695 (2003).

14. S. Raghavan, T. Schumann, H. Kim, J. Y. Zhang, T. A. Cain, and S. Stemmer, "High-mobility BaSnO$_3$ grown by oxide molecular beam epitaxy," APL Mater. **4**, 016106 (2016).

15. R. A. McKee, F. J. Walker, and M. F. Chisholm, "Physical structure and inversion charge at a semiconductor interface with a crystalline oxide," Science **293**, 468–471 (2001).

16. C. Dubourdieu, J. Bruley, T. M. Arruda, A. Posadas, J. Jordan-Sweet, M. M. Frank, E. Cartier, D. J. Frank, S. V. Kalinin, A. A. Demkov, and V. Narayanan, "Switching of ferroelectric polarization in epitaxial BaTiO$_3$ films on silicon without a conducting bottom electrode," Nat. Nanotechnol. **8**, 748–754 (2013).

17. B. W. Wessels, "Ferroelectric epitaxial thin films for integrated optics," Ann. Rev. Mater. Res. **37**, 659–679 (2007).

18. D. M. Gill, C. W. Conrad, G. Ford, B. W. Wessels, and S. T. Ho, "Thin-film channel waveguide electro-optic modulator in epitaxial BaTiO$_3$," Appl. Phys. Lett. **71**, 1783–1785 (1997).

19. Y. Garbovskiy and A. Glushchenko, "Optical/ferroelectric characterization of BaTiO$_3$ and PbTiO$_3$ colloidal nanoparticles and their applications in hybrid materials technologies," Appl. Opt. **52**, E34–E39 (2013).

20. M. K. Trivedi, G. Nayak, S. Patil, R. M. Tallapragada, O. Latiyal, and S. Jana, "Impact of biofield treatment on atomic and structural characteristics of barium titanate powder," Indus. Eng. Manage. **4**, 166 (2015).

21. P. T. Lin, Z. Liu, and B. W. Wessels, "Ferroelectric thin film photonic crystal waveguide and its electro-optic properties," J. Opt. A **11**, 075005 (2009).

22. A. Petraru, M. Siegert, M. Schmid, J. Schubert, and Ch. Buchal, "Ferroelectric BaTiO$_3$ thin film optical waveguide modulators," in *Ferroelectric Thin Films X*, Vol. **688** of MRS Symposium Proceedings (Cambridge University Press, 2002), pp. 279–284.

23. T. Zhao, H. Lu, F. Chen, G. Yang, and Z. Chen, "Stress-induced enhancement of second-order nonlinear optical susceptibilities of barium titanate films," J. Appl. Phys. **87**, 7448–7451 (2000).

24. M. B. Lee, M. Kawasaki, M. Yoshimoto, and H. Koinuma, "Heteroepitaxial growth of BaTiO$_3$ films on Si by pulsed laser deposition," Appl. Phys. Lett. **66**, 1331–1333 (1995).

25. M. H. M. Hsu, D. Van Thourhout, M. Pantouvaki, J. Meersschaut, T. Conard, O. Richard, H. Bender, P. Favia, M. Vila, and R. Cid, "Controlled orientation of molecular-beam-epitaxial BaTiO$_3$ on Si (001) using thickness engineering of BaTiO$_3$ and SrTiO$_3$ buffer layers," Appl. Phys. Express **10**, 065501 (2017).

26. T. Zhao, Z. H. Chen, F. Chen, W. S. Shi, H. B. Lu, and G. Z. Yang, "Enhancement of second-harmonic generation in BaTiO$_3$/SrTiO$_3$ superlattices," Phys. Rev. B **60**, 1697–1700 (1999).

27. E. Kim, A. Steinbrück, M. T. Buscaglia, V. Buscaglia, T. Pertsch, and R. Grange, "Second-harmonic generation of single BaTiO$_3$ nanoparticles down to 22 nm diameter," ACS Nano **7**, 5343–5349 (2013).

28. B. Bihari, J. Kumar, G. T. Stauf, P. C. Van Buskirk, and C. S. Hwang, "Investigation of barium titanate thin films on MgO substrates by second-harmonic generation," J. Appl. Phys. **76**, 1169–1174 (1994).

29. F. Capasso, R. Paiella, R. Martini, R. Colombelli, C. Gmachl, T. L. Myers, M. S. Taubman, R. M. Williams, C. G. Bethea, K. Unterrainer, H. Y. Hwang, D. L. Sivco, A. Y. Cho, A. M. Sergent, H. C. Liu, and E. A. Whittaker, "Quantum cascade lasers: ultrahigh-speed operation, optical wireless communication, narrow linewidth, and far-infrared emission," IEEE J. Quantum Electron. **38**, 511–532 (2002).

30. P. T. Lin, H.-Y. G. Lin, Z. Han, T. Jin, R. Millender, L. C. Kimerling, and A. Agarwal, "Label-free glucose sensing using chip-scale mid-infrared integrated photonics," Adv. Opt. Mater. **4**, 1755–1759 (2016).

31. D. Farrah, J. Bernard-Salas, H. W. W. Spoon, B. T. Soifer, L. Armus, B. Brandl, V. Charmandaris, V. Desai, S. Higdon, D. Devost, and J. Houck, "High-resolution mid-infrared spectroscopy of ultraluminous infrared galaxies," Astrophys. J. **667**, 149–169 (2007).

32. P. R. Christensen, B. M. Jakosky, H. H. Kieffer, M. C. Malin, H. Y. McSween, Jr., K. Nealson, G. L. Mehall, S. H. Silverman, S. Ferry, M. Caplinger, and M. Ravine, "The thermal emission imaging system (THEMIS) for the Mars 2001 Odyssey Mission," Space Sci. Rev. **110**, 85–130 (2004).

33. T. Jin, J. Zhou, H.-Y. Lin, and P. T. Lin, "Mid-infrared chalcogenide waveguides for real-time and non-destructive volatile organic compounds detection," Anal. Chem. **91**, 817–822 (2018).

34. J. Zhou and P. T. Lin, "Mid-infrared multi-spectral detection for real-time and non-invasive analysis of structure and composition of materials," ACS Sens. **3**, 1322–1328 (2018).

35. H. D. Megaw, "Origin of ferroelectricity in barium titanate and other perovskite-type crystals," Acta Crystallogr. **5**, 739–749 (1952).

36. S. A. Denev, T. T. A. Lummen, E. Barnes, A. Kumar, and V. Gopalan, "Probing ferroelectrics using optical second harmonic generation," J. Am. Ceram. Soc. **94**, 2699–2727 (2011).

37. O. Diéguez, K. M. Rabe, and D. Vanderbilt, "First-principles study of epitaxial strain in perovskites," Phys. Rev. B **72**, 144101 (2005).